Nanoscale

PAPER

View Article Online
View Journal | View Issue

Cite this: *Nanoscale*, 2018, **10**, 8585

Bio-inspired graphene-derived membranes with strain-controlled interlayer spacing†

Enlai Gao *[a] and Zhiping Xu *[a,b]

The precisely controlled size of nanoscale fluidic channels plays a critical role in resolving the permeation-selectivity trade-off in separation and filtration applications, where highly efficient gas separation and water desalination are targeted. Inspired by natural nacre where the spacing between mineral platelets changes upon applying tension as fractured mineral bridges climb over each other, bio-inspired graphene-derived membranes with sheets cross-linked by aligned covalent bonds are proposed in design, to ensure a controlled interlayer spacing ranging from 4 Å to 14 Å while preserving structural and mechanical stabilities by prohibiting swelling. The underlying mechanism is that the tension applied to the membrane is transferred between finite-sized graphene sheets through interlayer shear of the cross-links, which expands the interlayer gallery. First-principles calculations and continuum mechanics based model analysis are combined to explore the feasibility of this protocol, by considering the microstructures of graphene-derived membranes that have recently been demonstrated to offer exceptional performance in selective mass transport. The results show that the critical size range in molecular sieving is covered by this synergetic interface- and strain-engineering approach.

Received 2nd January 2018,
Accepted 28th March 2018

DOI: 10.1039/c8nr00013a

rsc.li/nanoscale

Introduction

The two-dimensional (2D) structures and engineerable physicochemical properties of graphene and its derivatives such as graphene oxide (GO) offer exciting opportunities in the design of molecular-sieving membranes by stacking 2D nanosheets layer by layer.[1–6] Typically, 40–60% total area of a GO sheet is free from oxygen-rich functionalization, and fast molecular permeation through graphene-derived membranes (GMs) was argued to occur along a percolated pathway of nearly-frictionless pristine graphene channels between functionalized areas.[7,8] The size of a GO channel is characterized by the distance h between the basal planes of GO sheets, or the void spacing $\delta = h - t$ that is defined through the interlayer spacing of graphite t = 3.4 Å, which quantifies the size exclusion effect in molecular sieving. For example, to reject sodium ions from water, the void spacing should be lower than the hydrated diameter of Na^+, 7.2 Å.[3,9] With the hydrophilic nature of GO, researchers reported that the GO membrane expands in the humid environment, and the interlayer spacing can be tailored in the range between 7 Å and 12 Å that is critical for gas separation and water desalination applications.[10–12] Other strategies have also been tried to engineer the interlayer spacing of GO membranes, including partial reduction,[13] ultraviolet reduction of a GO–titania hybrid,[14] capillary compression,[15,16] and hydrogen or coordinative bond assisted cross-linking.[17,18] However, the GO membranes disintegrate upon hydration owing to the electrostatic repulsion between negatively charged GO sheets, and swell while immersed in aqueous solutions.[19,20] It is thus challenging to control the interlayer spacing at a specific value in the nanometer range to selectively exclude ions such Na^+, K^+, Mg^{2+}, and Ca^{2+}, while maintaining the structural stability of membranes at the same time.[4,9] Moreover, reliable techniques for interlayer spacing tuning while the selective molecular transport process is active have not been discussed yet.

Also featuring a layer-by-layer microstructure (Fig. 1), nacre consists of 95 vol% of inorganic layered aragonite ($CaCO_3$) platelets (~200–500 nm thick) that are bonded by thin (~10–50 nm) layers of organic proteins and chitin. This natural composite exhibits the synergy between strengthening and toughening through the staggered arrangement of platelets and bonding layers, with the structural hierarchy established through the evolution over billions of years,[21] which has been regarded as a fruitful source of inspiration in designing high-performance and multifunctional materials,[22–24] and significant advances have been achieved in engineering the inter-

[a]*Applied Mechanics Laboratory, Department of Engineering Mechanics and Center for Nano and Micro Mechanics, Tsinghua University, Beijing 100084, China. E-mail: xuzp@tsinghua.edu.cn, enlaigao@gmail.com*
[b]*Applied Mechanics and Structure Safety Key Laboratory of Sichuan Province, School of Mechanics and Engineering, Southwest Jiaotong University, Chengdu 611756, China*

† Electronic supplementary information (ESI) available: Fig. S1 and S2. See DOI: 10.1039/c8nr00013a

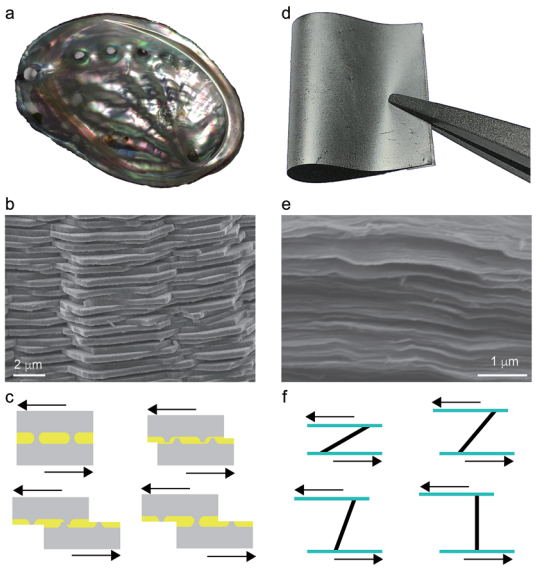

Fig. 1 Natural nacre and the GM. (a) Optical image of the nacre. (b) The electron micrograph of the nacre, showing the staggered arrangement of $CaCO_3$ platelets in the layered composite. (c) Shear within the organic matrix as the shell is stretched.[25] The mineral bridges in the overlap regions deform and fracture upon tensile loading. The two fractured sides of mineral bridges intrude into the organic matrix, levelly sliding along the opposite direction, and eventually climbed over each other, leading to an increase in the interlayer spacing between the platelets. (d) Optical image of the GM. (e) The electron micrograph showing the cross-section of a GM with stacked GO sheets. (f) Snapshots of design demonstrating structural evolution upon applying interlayer shear in a GM where the cross-links rotate and the interlayer spacing increases.

face of GMs by incorporating covalent bonding and non-covalent bonding (hydrogen bonding, ionic bonding, and π–π interaction) to enhance the overall stiffness, strength, toughness and fatigue resistance.[25–37] Recent studies revealed that the interlayer spacing between the mineral platelets increases with longitudinal strain within a critical range, which is attributed to the climbing of fractured mineral bridges between the neighboring platelets, as illustrated in Fig. 1c.[38]

Although advances have been achieved in engineering the interface of graphene-based films with various cross-links experimentally, the cross-links should be stiff and strong enough to maintain the structural stability of the interlayer gallery with a specific interlayer spacing. We thus considered short covalent cross-links to endow the GMs with interface- and strain-engineered interlayer spacing, which were identified experimentally in graphite[39] and carbon nanotube bundles[40] as a result of the vacancy aggregation under irradiation, known also as the extended inter-planar linking (EIL) structures.[41] We explored the structural and mechanical responses of a supercell with covalently cross-linked graphene sheets by performing first-principles calculations. The results are fed into the deformable tension-shear (DTS) model to analyze the overall behaviors of the GM, through a representative volume element (RVE). We find that the interlayer spacing can be tuned by uniaxial tensile loading in parallel to the GO sheets through interlayer shear or rotation of the cross-linking units, while the amplitude of the response depends on the microstructural parameters including the size of GO sheets, type and density of the cross-links, leading to a wide range of interlayer spacing under control from 4 Å to 14 Å, which is critical for designing high-performance membranes for nanoscale selective mass transport.

Methods

The structural and mechanical responses of cross-linked GMs are calculated using the plane-wave basis set based density functional theory (DFT) as implemented in the Vienna *ab initio* simulation package (VASP), with the projector augmented wave (PAW) method used for the ion–electron interaction and the Perdew–Burke–Ernzerhof parameterization (PBE)[42] of the generalized gradient approximation (GGA) for the exchange–correlation functional. The cross-linked GM is modeled by a supercell with lateral dimensions of 19.7 Å and 17.1 Å along the zigzag and perpendicular armchair directions, loaded under simple shear by moving one graphene sheet with respect to its next neighbor step by step. After each rigid displacement, the atomic structures of the supercell are relaxed while all the atomic degrees of freedom are constrained in the loading direction. The interlayer shear force is calculated by summing up all the forces acting on the carbon atoms of each graphene sheet in the loading direction. More computational details are described in our previous work.[50]

Results and discussion

Fig. 1a and d present the optical images of natural nacre and the GM constructed from the GO sheets. Fig. 1b and e show scanning electron micrographs of their characteristic brick-and-mortar microstructures. In nacre, the inorganic $CaCO_3$ platelets with mineral bridges connecting each other are the 'bricks', glued by the organic 'mortar'. Considering the finite size of $CaCO_3$ platelets, the in-plane tension applied has to be transferred across the neighboring platelets through shear within the interlayer organic matrix. The mineral bridges in the overlap regions deform and fracture upon tensile loading. The two fractured sides of the mineral bridges intrude into the organic matrix, levelly sliding along the opposite direction, and eventually climbed over each other, leading to an increase in the interlayer spacing between platelets (Fig. 1c).[38]

Inspired by this layered-hierarchy-enabled mechanism and without the loss of generality, we designed GMs with graphene sheets cross-linked by three EIL structures (C1, C2, C3) with lengths of $2b$, $5b$ and $8b$, measured in unit of the carbon–carbon bond length b = 1.42 Å (Fig. 2b). In these cross-linked structures, 6, 10, and 14 carbon atoms in graphene sheets are removed to create vacancy defects for bond reconstruction processes required to form the cross-links. Structural and

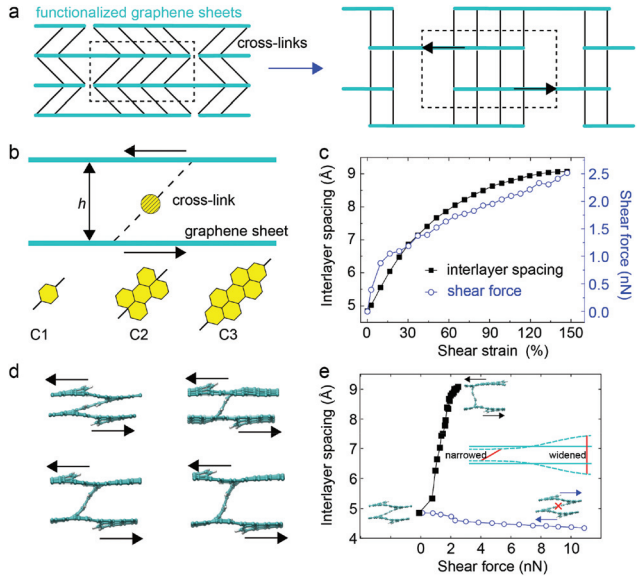

Fig. 2 Mechanisms of strain-engineered interlayer spacing. (a) The deformable tensile-shear (DTS) model, and the representative volume element (RVE), before and after tensile loading is applied. The interlayer spacing increases with tensile strain and thus exhibits negative Poisson's effect. (b) Detailed atomic structures of the three cross-links with varied lengths, named C1, C2 and C3. (c) Responses in the interlayer spacing and shear force as shear strain is applied. (d) First-principles simulation snapshots showing microstructural evolution of graphene sheets cross-linked by the C2 EIL structure. (e) The relationship between interlayer spacing and shear force for the C2-crosslinked structural unit rotated in the anticlockwise and clockwise directions.

mechanical responses of the cross-linked GMs are calculated using the plane-wave basis set based DFT (see Methods for details). The results are shown in Fig. S1,† which plot the relationship between the interlayer spacing h and shear strain γ for all the three types of cross-links. As summarized in Fig. S2,† the interfacial shear strength of a single C1, C2 or C3 cross-link is ~13 nN. As illustrated in Fig. 2c and d by the simulation snapshots of C2, it is clear that, working as designed, both F and h can be continuously tuned through γ before reaching the shear strain corresponding to the peak interlayer spacing. Specifically, for the C2 structure, the interlayer spacing of a GM can thus be controlled in the range from 4.8 Å to 9.1 Å with shear strain applied from 0 to 150%, while the ranges of interlayer spacing for C1 and C3 structures are 4.1 Å–4.5 Å and 5.8 Å–14.1 Å, respectively (Fig. S1 of the ESI†). It should be noted that shear and sliding at non-covalent interfaces between graphite,[43,44] nanotubes[45–47] and cellulose nanocrystals[48,49] were widely explored, but little has been mentioned about microstructural tailoring that results in and finely-tuned interlayer distances in a wide range under mechanical loading while the structural stability of the interlayer gallery is maintained at the same time.

Considering the fact that in fabricating the GM, the orientation of the cross-links may not be well controlled at the molecular scale, we explore the response in interlayer spacing with cross-links (C2 as a representative structure) in two opposite directions (Fig. 2e). DFT calculation results show that the interlayer spacing increases by 87.1%, while it decreases by only 11.4% as the load is applied in anticlockwise and clockwise directions. The response is thus asymmetric and the swelling amplitude is more prominent than that of shrinking under the shear force of the same amplitude in opposite directions. As the GM is under loading, there are regions expanded or shrunk, forming wide and narrow channels within the interlayer gallery (Fig. 2e, inset). However, the interlayer spacing for the narrow channel is less than the initial value of 4.8 Å, corresponding to the effective void spacing which is less than 1.4 Å (Fig. 2e), which is too narrow to transport ions and water molecules. Hence, the widened channels control the process of rejection. According to these facts, we limit our following discussion to the situation where all cross-links aligned in the direction with the maximum response that increases interlayer spacing upon tensile loading (Fig. 2a). In addition, the cross-links that rotate in the clockwise direction under loading exhibit a brittle nature, with much higher interlayer shear stiffness while lower shear strain to failure than those of the ductile cross-links that rotate in the anticlockwise direction (Fig. S3 of the ESI†). This contrast is attributed to the competition between bending and stretching of these two types of cross-links under shear, which could inspire stiffening and toughening strategies for the GMs.

To map the response of a single cross-linked structural unit loaded with shear to a graphene-derived membrane with a specific number of cross-links under tension, we consider the brick-and-mortar structure of GMs in our RVE of DTS with uniformly-distributed cross-links, where the areal density ϕ is defined as N_V/N_C. N_C is the number of carbon atoms in pristine graphene and N_V is the number of atoms removed to form the cross-link. As a result, we have $D = D_0(1 - \alpha\phi)$ and $\sigma_{cr} = \sigma_c/(1 + \beta\phi)^{0.5}$, where D_0 and σ_c are the tensile stiffness and strength of the pristine graphene sheet, and α, β are the numeric factor calculated for the mono-vacancies.[50] In addition, the effective interlayer shear modulus G scales linearly with ϕ as $G = k\phi/(N_V f)$. Here $f = 0.026$ nm^2 is the area of each carbon atom in the graphene sheet. By virtue of the DTS model (Fig. S4 of the ESI†) where the interlayer cross-links are considered as continuum media under the shear that transfers tensile loads carried by neighboring graphene sheets,[50–52] we analyze the overall mechanical response of the GM and the change of interlayer spacing under uniaxial tension. The in-plane displacements of the two graphene layers are denoted as $u_1(x)$ and $u_2(x)$, where x is the in-plane coordinate measured along the tensile loading direction. For the two graphene sheets in the structural unit, the equilibrium equations are

$$D\frac{\partial^2 u_1(x)}{\partial x^2} = 2G\frac{u_1(x) - u_2(x)}{h_0} \quad (1a)$$

$$D\frac{\partial^2 u_2(x)}{\partial x^2} = 2G\frac{u_2(x) - u_1(x)}{h_0} \quad (1b)$$

Combining the boundary conditions

$$D\frac{\partial u_1(0)}{\partial x}=0,\ D\frac{\partial u_1(l)}{\partial x}=F_0,\ D\frac{\partial u_2(0)}{\partial x}=F_0 \text{ and } D\frac{\partial u_2(l)}{\partial x}=0,$$

the displacements can be solved as

$$u_1(x)=\frac{1}{2}\left(C+\frac{F_0}{D}x+\frac{F_0 l_0}{D}\sinh\frac{x}{l_0}+\frac{F_0 l_0}{D}\frac{1+c}{s}\cosh\frac{x}{l_0}\right) \quad (2a)$$

$$u_2(x)=\frac{1}{2}\left(C+\frac{F_0}{D}x-\frac{F_0 l_0}{D}\sinh\frac{x}{l_0}-\frac{F_0 l_0}{D}\frac{1+c}{s}\cosh\frac{x}{l_0}\right) \quad (2b)$$

Here $s=\sinh(l/l_0)$, $c=\cosh(l/l_0)$, F_0 is the applied tensile force, l is the lateral size of the RVE and thus $2l$ is the size of the graphene sheet. $l_0=(Dh_0/4G)^{1/2}$ is a characteristic length scale defining the effectiveness of interlayer load transfer between the neighboring sheets through the cross-links, where parameters D, G and h_0 are the tensile stiffness of the cross-linked graphene sheets, the effective shear modulus of the interlayer cross-links and the interlayer spacing before the tensile load is applied. From the analysis, we found that the tensile strain in the graphene sheet $\varepsilon_1(x)$, and shear strain between the neighboring sheets $\gamma_1(x)$ in a RVE can be derived as

$$\varepsilon_1(x)=\frac{F_0}{2D}\left[1-\cosh\left(\frac{x}{l_0}\right)+\frac{1+c}{s}\sinh\left(\frac{x}{l_0}\right)\right] \quad (3)$$

$$\gamma_1(x)=\frac{F_0 l_0}{Dh_0}\left[(1+c)\cosh\left(\frac{x}{l_0}\right)-s\times sinh\left(\frac{x}{l_0}\right)\right]/s \quad (4)$$

From $\gamma_1(x)$ one could evaluate the average shear strain γ ($0<x<l$) of interlayer cross-links, that is

$$\gamma=\int_0^l\frac{\gamma_1(x)}{l}\mathrm{d}x=\frac{2F_0 {l_0}^2}{Dh_0 l} \quad (5)$$

while the overall tensile strain of GMs can be expressed as a function of the interlayer spacing

$$\varepsilon(h)=[\gamma_1(0)h_0+\int_0^l\varepsilon_1(x)\mathrm{d}x]/l=\left(\frac{h_0}{2l_0}\frac{1+c}{s}+\frac{Gl}{D}\right)\gamma(h) \quad (6)$$

With the first-principles results for the relation between the shear strain γ and changes in the interlayer spacing h, the tunability of h through tensile strain ε can be assessed. It should be noted here that the amplitude of shear strain is not uniform along the sheet, as demonstrated in the DTS model.[30] However, we use the average shear strain (eqn (5)) to calculate the change in interlayer spacing according to our previous arguments on the size distribution of nanochannels. Using this model and relevant parameters determined from the DFT calculations, the results of changes in the interlayer spacing of GMs upon applying tensile strain ε are summarized in Fig. 3 for graphene sheets with lateral size $2l$ cross-linked by C1, C2 and C3 cross-links. From the results we conclude that the interlayer spacing of GMs can be finely tuned through the amplitude of tensile strain, the areal density of cross-linking, the size of graphene sheets, and the types of interlayer cross-links, according to eqn (6). The changes in the interlayer spacing are plotted before the peak value is reached upon

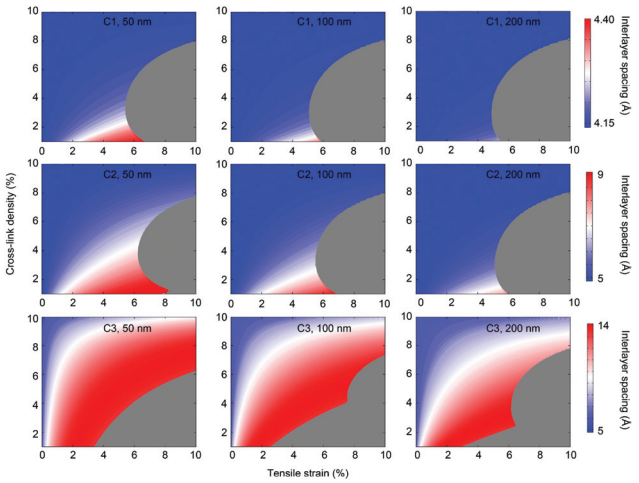

Fig. 3 Tensile strain-controlled interlayer spacing in the GMs, which are finely tuned by the areal density of C1, C2 and C3 cross-links and the size of graphene sheets (50 nm, 100 nm and 200 nm), under tensile strain loading.

loading, after which the spacing is reduced or structure fails, marked as the grey regions in Fig. 3. It can be seen that as the length of the crosslink increases from C1 to C3, the stiffness decreases and so does the applied tensile strain required to shear the crosslink to the upward configuration with the peak value of interlayer spacing.

For filtration and separation applications of GMs, the molecular sieving effect plays a central role in selecting the species to be permeable and determining their permeation rates, which decrease at reduced interlayer spacing (Fig. 4a).[2,3] Recent studies on the GO membrane reported that the ionic permeation rates of Na^+ and K^+ demonstrate the exponential dependence on the interlayer spacing, and decrease by two orders of magnitude as the interlayer spacing is reduced from 9.8 Å to 7.4 Å. In this experiment, spacing control is established by tuning the relative humidity, where the GO sheets

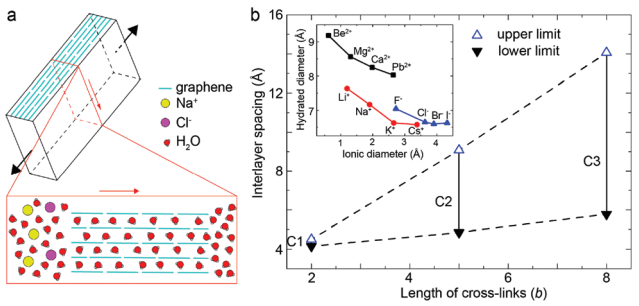

Fig. 4 The critical ranges of interlayer spacing in molecular-sieving processes. (a) The size-sieving mechanism in water desalination. (b) A summary of the hydrated ionic diameters and the range of strain-controllable interlayer spacing in the GMs as proposed in this work. The upper and lower limits correspond to the range of interlayer spacing tuned through strain (Fig. S1†). The critical size range in molecular sieving is covered by the strain-engineering approach.

are encapsulated in an epoxy film for stabilization.[3] In an aqueous environment, the ion–water interaction results in the formation of a hydrated $M^{z+}(H_2O)_n$ complex with n water molecules in the solvation shell of the M^{z+} ion, the size of which determines its permeability in the nanochannels. Fig. 4b summarizes the values of strain-controlled interlayer spacing h, which increase with the length of cross-links and range from 4 to 14 Å through C1-, C2- and C3-cross-linking. This range covers critical sizes of hydrated ions in the molecular sieving processes for water desalination (Fig. 4b, inset).[53] Moreover, the covalent nature of these cross-links maintain the structural and mechanical stabilities upon hydration and strain engineering, as the shear strain between graphene sheets is well below the tensile strain to failure (Fig. 3). In addition, cross-linking densities can also be tuned to optimize the mechanical performance such as stiffness, strength and resilience by balancing the intralayer and interlayer load transfer.[50]

Conclusions

In summary, bio-inspired graphene-derived membranes are designed in this work, with graphene sheets bonded by covalent interlayer cross-links. The rotation of cross-links results in the change of the interlayer gallery upon applying interlayer shear, induced by tensile strain applied to the membrane. This phenomenon can also be considered as a negative Poisson's ratio effect that has raised interest recently.[54–57] Our first-principles calculations and model analysis demonstrate that the interlayer spacing of the membrane can be well controlled and tuned in a critical range of tensile strain, which is highly promising in molecular sieving based filtration and separation applications, while the structural integrity and stability are well preserved at the same time.

Conflicts of interest

There are no conflicts to declare.

Acknowledgements

This work was supported by the Opening Project of Applied Mechanics and Structure Safety Key Laboratory of Sichuan Province through Grant SZDKF-1601, and the National Natural Science Foundation of China through Grant 11472150. The computation was performed on the Explorer 100 cluster system of the Tsinghua National Laboratory for Information Science and Technology.

References

1 C. Sealy, *Nano Today*, 2017, **14**, 1–2.
2 R. K. Joshi, P. Carbone, F. C. Wang, V. G. Kravets, Y. Su, I. V. Grigorieva, H. A. Wu, A. K. Geim and R. R. Nair, *Science*, 2014, **343**, 752–754.
3 J. Abraham, K. S. Vasu, C. D. Williams, K. Gopinadhan, Y. Su, C. T. Cherian, J. Dix, E. Prestat, S. J. Haigh, I. V. Grigorieva, P. Carbone, A. K. Geim and R. R. Nair, *Nat. Nanotechnol.*, 2017, **12**, 546–550.
4 L. Chen, G. Shi, J. Shen, B. Peng, B. Zhang, Y. Wang, F. Bian, J. Wang, D. Li, Z. Qian, G. Xu, G. Liu, J. Zeng, L. Zhang, Y. Yang, G. Zhou, M. Wu, W. Jin, J. Li and H. Fang, *Nature*, 2017, **550**, 380–383.
5 Z. Qin and M. J. Buehler, *Nano Lett.*, 2015, **15**, 3939–3944.
6 Q. Xie, F. Xin, H. G. Park and C. Duan, *Nanoscale*, 2016, **8**, 19527–19535.
7 N. R. Wilson, P. A. Pandey, R. Beanland, R. J. Young, I. A. Kinloch, L. Gong, Z. Liu, K. Suenaga, J. P. Rourke, S. J. York and J. Sloan, *ACS Nano*, 2009, **3**, 2547–2556.
8 K. P. Loh, Q. Bao, G. Eda and M. Chhowalla, *Nat. Chem.*, 2010, **2**, 1015–1024.
9 B. Mi, *Science*, 2014, **343**, 740–742.
10 A. Klechikov, J. Yu, D. Thomas, T. Sharifi and A. V. Talyzin, *Nanoscale*, 2015, **7**, 15374–15384.
11 A. V. Talyzin, T. Hausmaninger, S. You and T. Szabo, *Nanoscale*, 2014, **6**, 272–281.
12 B. Rezania, N. Severin, A. V. Talyzin and J. P. Rabe, *Nano Lett.*, 2014, **14**, 3993–3998.
13 H. Liu, H. Wang and X. Zhang, *Adv. Mater.*, 2015, **27**, 249–254.
14 P. Z. Sun, Q. Chen, X. D. Li, H. Liu, K. L. Wang, M. L. Zhong, J. Q. Wei, D. H. Wu, R. Z. Ma, T. Sasaki and H. W. Zhu, *NPG Asia Mater.*, 2015, **7**, e162.
15 C. Cheng, G. Jiang, C. J. Garvey, Y. Wang, G. P. Simon, J. Z. Liu and D. Li, *Sci. Adv.*, 2016, **2**, e1501272.
16 X. Yang, C. Cheng, Y. Wang, L. Qiu and D. Li, *Science*, 2013, **341**, 534–537.
17 X. Lin, X. Shen, X. Sun, X. Liu, Y. Wu, Z. Wang and J. K. Kim, *ACS Appl. Mater. Interfaces*, 2016, **8**, 2360–2371.
18 W.-S. Hung, C.-H. Tsou, M. De Guzman, Q.-F. An, Y.-L. Liu, Y.-M. Zhang, C.-C. Hu, K.-R. Lee and J.-Y. Lai, *Chem. Mater.*, 2014, **26**, 2983–2990.
19 C. N. Yeh, K. Raidongia, J. Shao, Q. H. Yang and J. Huang, *Nat. Chem.*, 2014, **7**, 166–170.
20 S. Zheng, Q. Tu, J. J. Urban, S. Li and B. Mi, *ACS Nano*, 2017, **11**, 6440–6450.
21 U. G. Wegst, H. Bai, E. Saiz, A. P. Tomsia and R. O. Ritchie, *Nat. Mater.*, 2015, **14**, 23–36.
22 Q. Cheng, J. Duan, Q. Zhang and L. Jiang, *ACS Nano*, 2015, **9**, 2231–2234.
23 H. L. Gao, S. M. Chen, L. B. Mao, Z. Q. Song, H. B. Yao, H. Colfen, X. S. Luo, F. Zhang, Z. Pan, Y. F. Meng, Y. Ni and S. H. Yu, *Nat. Commun.*, 2017, **8**, 287.
24 S. Wan, H. Hu, J. Peng, Y. Li, Y. Fan, L. Jiang and Q. Cheng, *Nanoscale*, 2016, **8**, 5649–5656.
25 W. Cui, M. Li, J. Liu, B. Wang, C. Zhang, L. Jiang and Q. Cheng, *ACS Nano*, 2014, **8**, 9511–9517.

26 S. Wan, J. Peng, Y. Li, H. Hu, L. Jiang and Q. Cheng, *ACS Nano*, 2015, **9**, 9830–9836.
27 S. Wan, Q. Zhang, X. Zhou, D. Li, B. Ji, L. Jiang and Q. Cheng, *ACS Nano*, 2017, **11**, 7074–7083.
28 J. Peng and Q. Cheng, *Adv. Mater.*, 2017, **29**, 1702959.
29 S. Wan, J. Peng, L. Jiang and Q. Cheng, *Adv. Mater.*, 2016, **28**, 7862–7898.
30 Y. Wen, M. Wu, M. Zhang, C. Li and G. Shi, *Adv. Mater.*, 2017, **29**, 1702831.
31 R. Xiong, K. Hu, A. M. Grant, R. Ma, W. Xu, C. Lu, X. Zhang and V. V. Tsukruk, *Adv. Mater.*, 2016, **28**, 1501–1509.
32 Y. Zhang, Y. Li, P. Ming, Q. Zhang, T. Liu, L. Jiang and Q. Cheng, *Adv. Mater.*, 2016, **28**, 2834–2839.
33 S. J. Wan, F. Y. Xu, L. Jiang and Q. F. Cheng, *Adv. Funct. Mater.*, 2017, **27**, 1605636.
34 Q. Cheng, M. Wu, M. Li, L. Jiang and Z. Tang, *Angew. Chem., Int. Ed.*, 2013, **52**, 3750–3755.
35 Y. Zhang, S. Gong, Q. Zhang, P. Ming, S. Wan, J. Peng, L. Jiang and Q. Cheng, *Chem. Soc. Rev.*, 2016, **45**, 2378–2395.
36 S. S. Gong, H. Ni, L. Jiang and Q. F. Cheng, *Mater. Today*, 2017, **20**, 210–219.
37 E. Gao, Y. Wen, Y. Yuan, C. Li and Z. Xu, *Carbon*, 2017, **118**, 467–474.
38 F. Song, J. Zhou, X. Xu, Y. Xu and Y. Bai, *Phys. Rev. Lett.*, 2008, **100**, 245502.
39 C. Karthik, J. Kane, D. P. Butt, W. E. Windes and R. Ubic, *J. Nucl. Mater.*, 2011, **412**, 321–326.
40 A. Kis, G. Csanyi, J. P. Salvetat, T. N. Lee, E. Couteau, A. J. Kulik, W. Benoit, J. Brugger and L. Forro, *Nat. Mater.*, 2004, **3**, 153–157.
41 T. Trevethan, P. Dyulgerova, C. D. Latham, M. I. Heggie, C. R. Seabourne, A. J. Scott, P. R. Briddon and M. J. Rayson, *Phys. Rev. Lett.*, 2013, **111**, 095501.
42 J. P. Perdew, K. Burke and M. Ernzerhof, *Phys. Rev. Lett.*, 1996, **77**, 3865–3868.
43 D. E. Soule and C. W. Nezbeda, *J. Appl. Phys.*, 1968, **39**, 5122–5139.
44 Z. Liu, J. Yang, F. Grey, J. Z. Liu, Y. Liu, Y. Wang, Y. Yang, Y. Cheng and Q. Zheng, *Phys. Rev. Lett.*, 2012, **108**, 205503.
45 N. M. Pugno, *J. Mech. Behav. Biomed. Mater.*, 2007, **18**, 265–281.
46 X. Zhang, in *Nanomechanics*, 2017, DOI: 10.5772/65466.
47 C. Li, Y. Liu, X. Yao, M. Ito, T. Noguchi and Q. Zheng, *Nanotechnology*, 2010, **21**, 115704.
48 R. Sinko and S. Keten, *J. Mech. Phys. Solids*, 2015, **78**, 526–539.
49 X. Wu, R. J. Moon and A. Martini, *Tribol. Lett.*, 2013, **52**, 395–405.
50 E. Gao, Y. Cao, Y. Liu and Z. Xu, *ACS Appl. Mater. Interfaces*, 2017, **9**, 24830–24839.
51 Y. L. Liu and Z. P. Xu, *J. Mech. Phys. Solids*, 2014, **70**, 30–41.
52 Y. L. Liu, B. Xie, Z. Zhang, Q. S. Zheng and Z. P. Xu, *J. Mech. Phys. Solids*, 2012, **60**, 591–605.
53 B. Tansel, *Sep. Purif. Technol.*, 2012, **86**, 119–126.
54 J. Wan, J. W. Jiang and H. S. Park, *Nanoscale*, 2017, **9**, 4007–4012.
55 C. Huang and L. Chen, *Adv. Mater.*, 2016, **28**, 8079–8096.
56 J. N. Grima, S. Winczewski, L. Mizzi, M. C. Grech, R. Cauchi, R. Gatt, D. Attard, K. W. Wojciechowski and J. Rybicki, *Adv. Mater.*, 2015, **27**, 1455–1459.
57 G. N. Greaves, A. L. Greer, R. S. Lakes and T. Rouxel, *Nat. Mater.*, 2011, **10**, 823–837.

Electronic Supplementary Material (ESI) for Nanoscale.
This journal is © The Royal Society of Chemistry 2018

Supplementary Information for

Bio-Inspired Graphene-Derived Membranes with Strain-Controlled Interlayer Spacing

Enlai Gao[a,*] and Zhiping Xu[a,b,*]

[a]Applied Mechanics Laboratory, Department of Engineering Mechanics and Center for Nano and Micro Mechanics, Tsinghua University, Beijing 100084, China.

[b]Applied Mechanics and Structure Safety Key Laboratory of Sichuan Province, School of Mechanics and Engineering, Southwest Jiaotong University, Chengdu 611756, China

[*]Corresponding authors, email: enlaigao@gmail.com, xuzp@tsinghua.edu.cn

The Supporting Materials contain

- Supplementary Figures S1-S4.

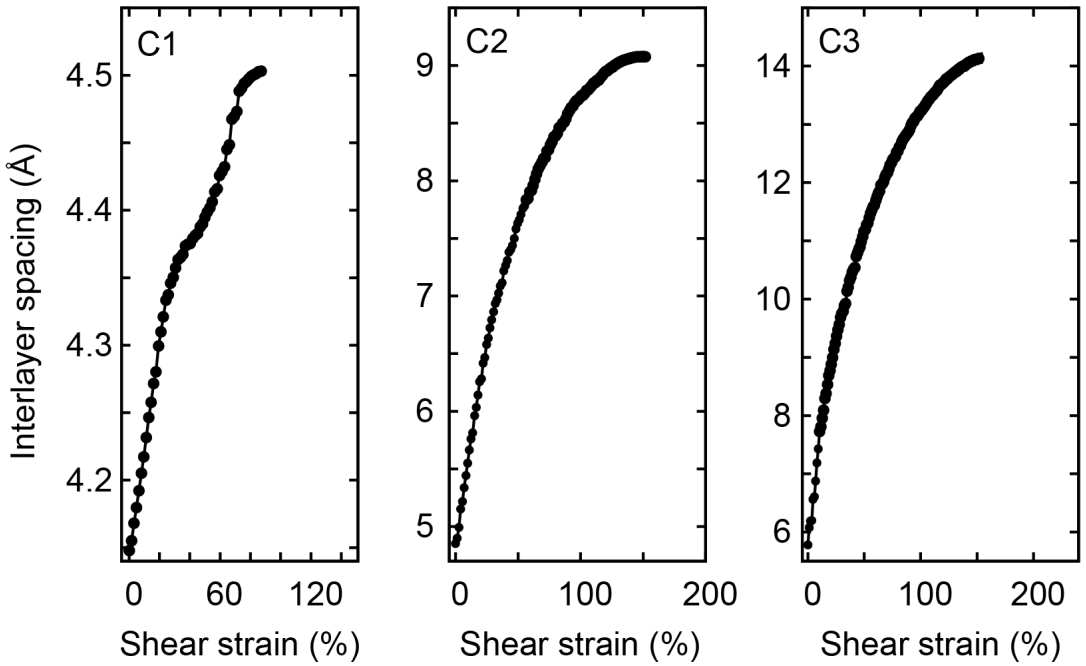

Figure S1 The relation between interlayer spacing and shear strain calculated from DFT calculations, for supercells with three types of interlayer cross-links (C1, C2 and C3).

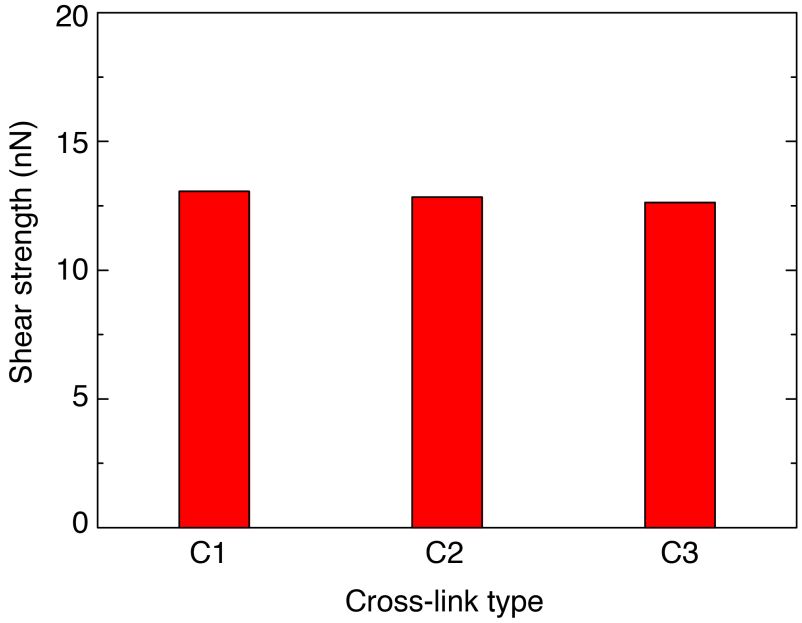

Figure S2 The interfacial shear strength for graphene sheets cross-linked by C1, C2 and C3 structures, respectively.

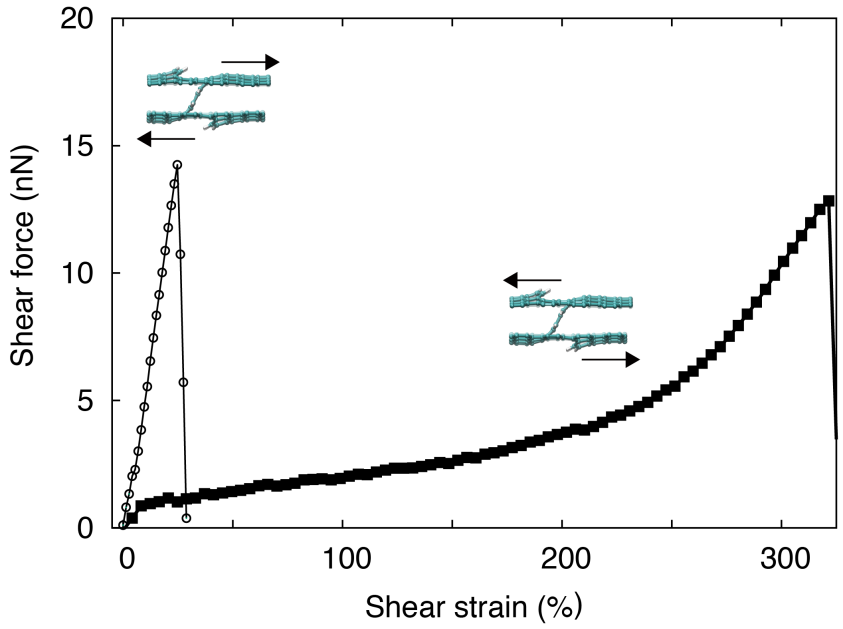

Figure S3 The shear force-strain relation calculated from DFT calculations for graphene sheets cross-linked by the C2 cross-links that rotate clockwisely and anticlockwisely, respectively.

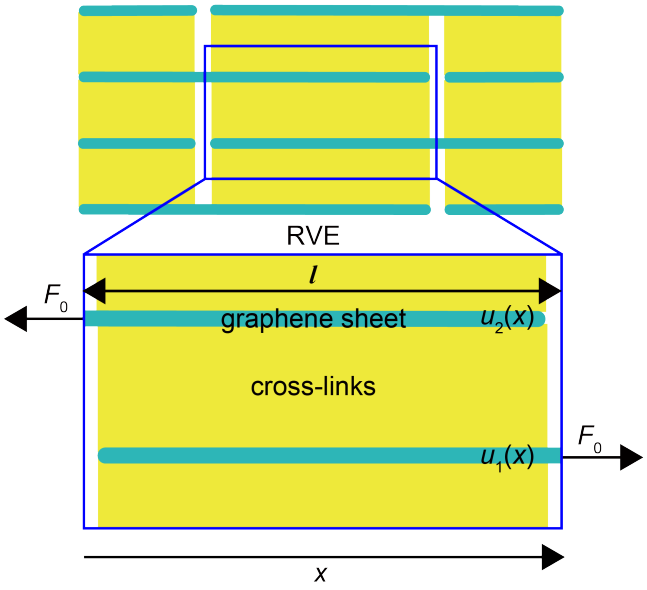

Figure S4 A schematic illustration of the RVE used in the DTS model, where graphene sheets are crosslinked.